



Al-mubarak, H., Vallatos, A., Gallagher, L., Birch, J., Chalmers, A.J. and Holmes, W.M. (2021) Evaluating potential of multi-parametric MRI using co-registered histology: Application to a mouse model of glioblastoma. *Magnetic resonance imaging*, 85, pp. 121-127.
(doi: [10.1016/j.mri.2021.10.030](https://doi.org/10.1016/j.mri.2021.10.030))

There may be differences between this version and the published version.
You are advised to consult the published version if you wish to cite from it.

<http://eprints.gla.ac.uk/258503/>

Deposited on 20 January 2022

Enlighten – Research publications by members of the University of Glasgow
<http://eprints.gla.ac.uk>

Evaluating potential of multi-parametric MRI using co-registered histology: Application to a mouse model of Glioblastoma.

H. Al-Mubarak^{a,b*}, A. Vallatos^c, L. Gallagher^a, J. Birch^d, A. J. Chalmers^e, W.M. Holmes^a

^aGlasgow Experimental MRI centre, Institute of Neuroscience and Psychology, University of Glasgow, G61 1QH, U.K.

^bDepartment of Physics, College of science, University of Misan, Iraq.

^cCentre for Clinical Brain Sciences, University of Edinburgh, EH16 4SB ,UK.

^dBeatson Institute for Cancer Research ,UK.

^eWolfson Wohl Translational Cancer Research Centre, Institute of Cancer Sciences University of Glasgow, G61 1QH, UK.

*Haitham Al-Mubarak e-mail: haitham_f99@outlook.com or haitham_f99@yahoo.com

Antoine Vallatos e-mail: antoine.vallatos@ed.ac.uk.

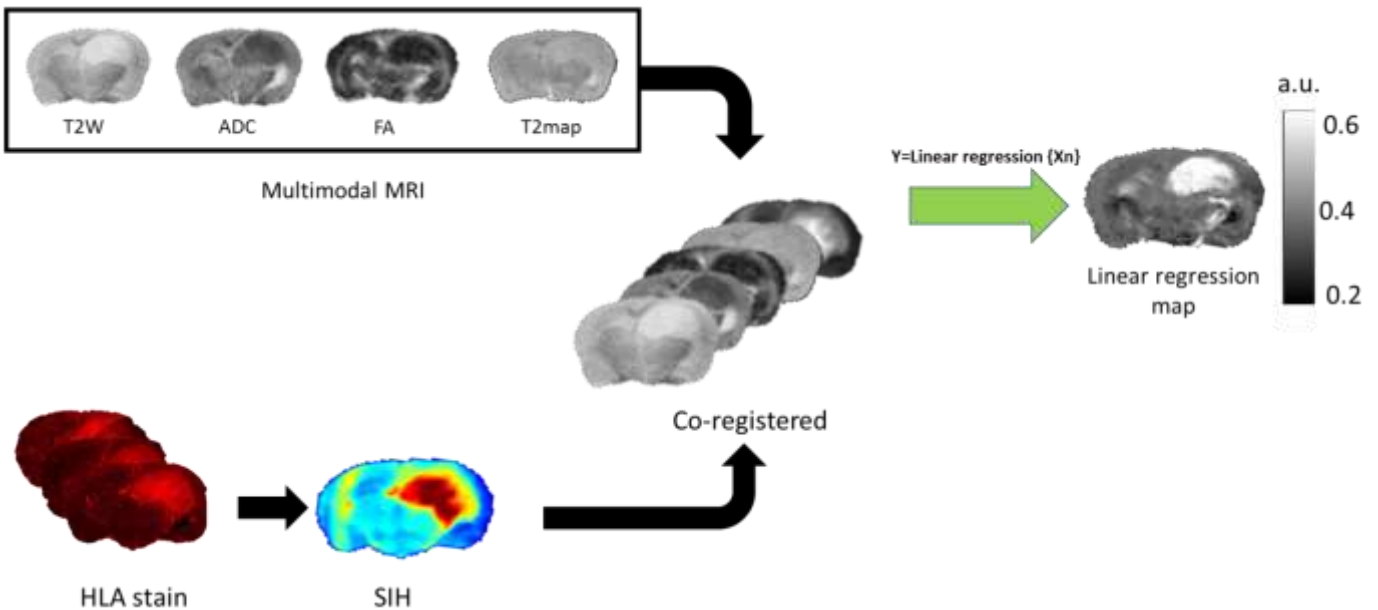
Lindsay Gallagher e-mail: Lindsay.Gallagher@ glasgow.ac.uk

Joanna Birch e-mail : j.birch@beatson.gla.ac.uk

Anthony Chalmers e-mail: Anthony.Chalmers@glasgow.ac.uk

William Holmes e-mail: william.Holmes@glasgow.ac.uk

Graphical abstract



30
31
32
33
34
35
36

37 **Abstract**

38 **Purpose:** MRI is capable of generating a range of image contrasts which are commonly assessed individually
39 by qualitative visual inspection. It has long been hypothesized that better diagnoses could be achieved by
40 combining these multiple images, so called multi-parametric or multi-spectral MRI. However, the lack of clinical
41 histology and the difficulties of co-registration, has meant this hypothesis has never been rigorously tested.
42 Here we test this hypothesis, using a previously published multi-dimensional dataset consisting of registered
43 MR images and histology.

44 **Methods:** To that effect, we set out to examine a registered dataset of MR images and histology from mice
45 bearing orthotopic glioblastoma xenografts generated from a patient-derived glioblastoma cell line. MRI was
46 performed at 7T consisting of T₁/T₂ weighted, T₂ mapping, contrast enhanced T₁, diffusion-weighted, diffusion
47 tensor imaging. Immunohistochemistry sections were cut in the MRI plane and stained for Human Leukocyte
48 Antigen (probing human-derived tumour cells). To achieve quantitative MRI-tissue comparison, multiple
49 histological sections were stacked to produce tumour cell density maps acting as 'ground truth'. Sensitivity,
50 specificity, accuracy and Dice similarity indices were calculated. ANOVA, *t*-test and Pearson coefficients were
51 used for statistical analysis.

52 **Results:** Correlation coefficient analysis with co-registered 'ground truth' histology showed interactive
53 regression maps had higher correlation coefficients and sensitivity values than T2W, ADC, FA, and T2 maps.
54 Further, the interaction regression maps showed statistical improved detection of tumour volume.

55 **Conclusion:** Voxel-by-voxel analysis provided quantitative evidence confirming the hypothesis that multi-
56 parametric MRI can, potentially, better distinguish between the tumour region and normal tissue.

57 **Key words:** Glioblastoma, Multi-parametric MRI, mpMRI, Linear regression, Infiltration, co-
58 registration.

59
60
61
62
63
64
65
66
67
68
69

70 1. Introduction

71

72 Magnetic Resonance Imaging has proven to be a powerful tool in clinical diagnosis. Clinical
73 MRI is capable of generating a range of image contrasts (e.g. T1W, T2W, DWI, FLAIR and
74 Gd-T1) which are commonly assessed individually by qualitative visual inspection [1, 2].
75 However, it has long been hypothesized that better diagnoses could be achieved by
76 combining these multiple images, so called multi-parametric or multi-spectral MRI. However,
77 this hypothesis has never been rigorously tested [3].

78 It is generally agreed that histopathology is the gold standard for characterising diseased
79 tissue and for validating imaging biomarkers [4]. For human patients this is limited to biopsy
80 (e.g. brain tumour) or post mortem specimens (e.g. carotid plaques [5]), which are cut into
81 thin sections and stained to reveal complex differentiated structures at the cellular level [6].
82 Even then, the localization/registration of histology sections with MR images is very
83 challenging.

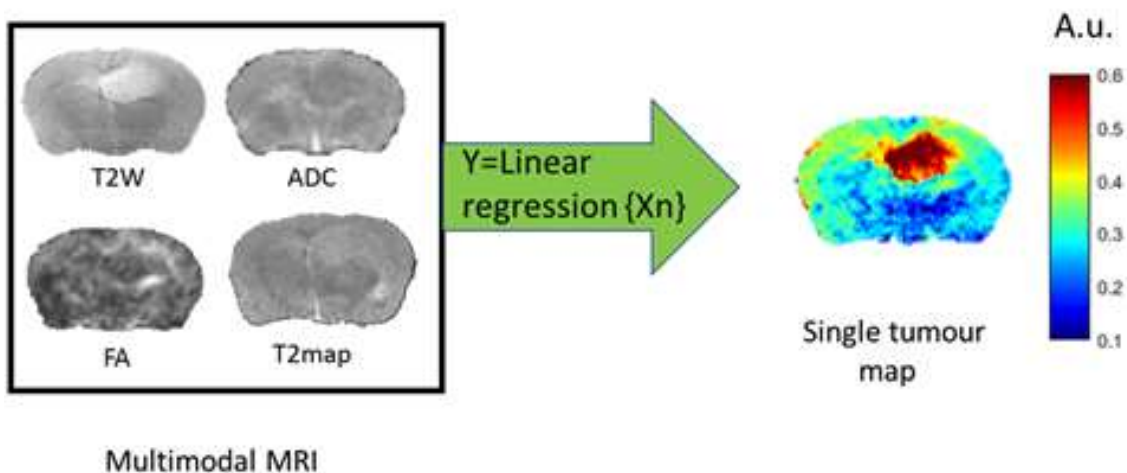
84 In the absence of histopathology, there are currently two strategies to analyze mpMRI data.
85 The first involves extracting relevant features such as volume, signal intensity and texture,
86 then applying a model to those factors [7-9]. The second strategy is to perform a voxel-wise
87 (voxel by voxel) analysis [10-12], transforming voxel values from each imaging modality to
88 create a single image map by applying either a linear or non-linear function.

89 GBM brain tumours are heterogeneous in nature, with GBM cells infiltrating into adjacent
90 normal tissue [13, 14]. For surgical resection and radiotherapy, planning is important to
91 accurately identify the outer boundary of this infiltration [15]. It is widely acknowledged that
92 conventional MRI (T1W, T2W, ADC, Gd-T1) cannot detect GBM infiltration beyond the
93 contrast enhanced region of Gd-T1 images. It has been speculated that the combination of
94 image data from various MRI modalities (morphological, functional and metabolic) has the
95 potential to provide the radiologist with a single tumour map (Fig.1) by extracting more
96 information from the individual images.

97 An example of the voxel-wise approach is the work of Fathi Kazerooni, Mohseni [3], who
98 proposed that using a combination of MRI images (ADC, PWI and T2W), followed by a
99 segmentation method, could identify the extent of GBM infiltration and help in its delineation
100 before surgery. Further, several studies have recommended including additional imaging

101 biomarkers adopted from diffusion and perfusion modalities [16-18]. However, these clinical
102 studies lack direct verification with the commonly agreed gold standard of histology.

103 Even when studying animal models of disease, where the animal can be readily sacrificed,
104 the comparison between MR images and histology sections has been mostly qualitative and
105 largely limited by the difficulties of co-registration. However, in a recent publication we
106 achieved high quality registration of histology with MRI, not by improving on current image
107 registration algorithms but by focusing on improving the quality of the histology sections [19].
108 We applied this stacked in-plane histology (SIH) methodology to a mouse model of GBM,
109 which resulted in a registered multi-dimensional datasets of MR images and histology. This
110 allowed a direct voxel-by-voxel assessment of individual MRI modalities, which found that
111 invasion of tumour cells can be detected beyond the edematous region by using a perfusion
112 weighted image (ASL) [18]. In this paper, we describe how we further interrogated this
113 unique dataset to quantitatively test the hypothesis that, by combining data from individual
114 MRI modalities, multi-parametric MRI has the potential to improve tumour detection.



115

116 **Figure 1: Reconstruction of a single tumour map from different MRI modalities when combined with**
117 **linear regression analysis.**

118

119 **2. Methods and Materials**

120 In this study we used a previously published multi-dimensional dataset consisting of
121 registered MR images and histology from a mouse model of GBM [18, 19]. The methods
122 used in acquiring this dataset are summarized below.

123

124

125 **2.1 Animal Preparation**

126

127 Ten immunocompromised CD1 nude mice (20-25g, Charles River Laboratories) were
128 intracranially injected the G7 Glioblastoma model (10^5 cells per mouse) derived from a
129 primary human tumour cell line. This cell line produces a tumour bulk with invasive edges *in*
130 *vivo* that replicates the human disease. For the MRI session, the mouse was anaesthetized
131 with 5% isoflurane for induction at 30:70 O₂/N₂O ratio. Next, the mouse was placed in the
132 MRI cradle and, using isoflurane at 2%, maintained using a 40:60 ratio of O₂/N₂O (1 L min⁻
133 ¹). The head of the mouse was restrained with both ear and tooth bars to prevent movement
134 during scanning. A rectal probe was used to monitor body temperature, which was
135 maintained at 37 ± 1 °C by an enclosed water circuit that surrounded the mouse. Experiments
136 were carried out under license from the UK Home Office in accordance with the *Animals*
137 *(Scientific Procedures) Act, 1986*, incorporating *European Directive 2010/63/EU* and
138 approved by the University of Glasgow Ethical Review Panel.

139 **2.2 MRI acquisitions**

140

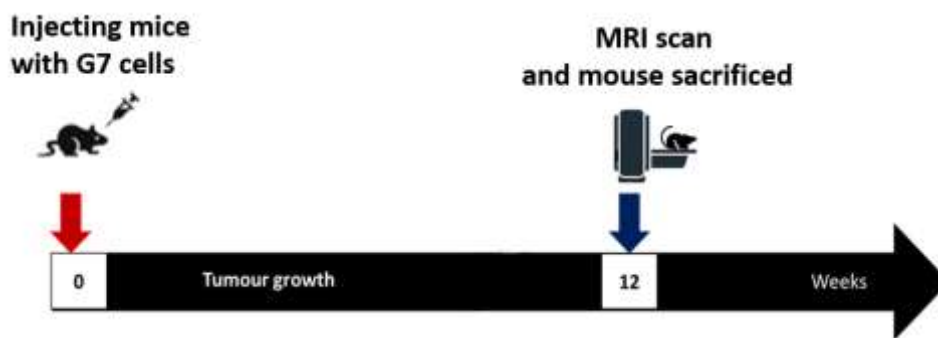
141 MRI experiments were performed on a Bruker Biospec Avance 7T imaging system (Bruker
142 Biospin, Ettlingen, Germany). Radiofrequency excitation was achieved using a 72mm
143 diameter birdcage volume resonator, with the signal detected using an actively decoupled
144 4-channel phased array receive-only head surface coil (Rapid Biomedical, Wurzburg,
145 Germany). MRI was performed with a field-of-view 2x2 cm on five 1.5 mm thick coronal
146 slices centered at 4 mm posterior from the rhinal fissure. T2 mapping was performed using
147 a Multi-Slice Multi-Echo (MSME) sequence (TE= 10 ms, TR=4394 ms, matrix 176x176, FOV
148 2 x 2cm, slice thickness=1.5mm). The signals from 15 echoes were acquired, giving 15
149 images of increasing effective echo-time. T2 maps were generated by fitting the signal decay
150 curve from each voxel with a single-exponential function (plus a baseline offset) using in-
151 house MATLAB script.

152

153 T2-weighted imaging was conducted using a Rapid Acquisition Relaxation Enhanced
154 (RARE) sequence (TE=47 ms, TR=4300 ms, matrix = 176x176, FOV = 2 x2 cm, slice
155 thickness=1.5mm, 7min). Diffusion-weighted imaging (DWI) was conducted using a 4-shot

156 spin-echo echo planar imaging DWI scan (TE=37.63 ms, TR=4,500 ms, matrix=128×128,
157 FOV 2 x 2cm, 1.5 mm slice thickness, 6 directions, b-values = 0, 1000 s.mm⁻², 10 min).
158 Contrast-enhanced T1 imaging (CE-T1) was conducted using a RARE acquisition (TE=12.3
159 ms, TR=800 ms, matrix=176×176, 8 min). Images were acquired before and 5 min after
160 Gadolinium-DTPA injection. In the last scanning sessions, T2W_{histology} experiments with 9
161 slices (slice thickness=0.5 mm) were also carried out with a RARE sequence (TE = 46 ms,
162 TR=5000 ms, matrix=176×176, 9 min, RARE factor = 8). Following *in vivo* scanning, a doped
163 water phantom was scanned to correct the sensitivity bias of the RF surface receiver coil.

164 Figure 2 shows the experimental protocol. At the conclusion of the MRI session, animals
165 were euthanized immediately and brains were removed and fresh-frozen. Histology sections
166 were then cut in the same plane as the MRI and stained using Human Leukocyte Antigen
167 (HLA) to identify the human tumour cells.



168

169 **Figure 2: Experimental protocol. At week zero, 10 mice were orthotopically implanted with G7**
170 **glioblastoma cells. Mice were imaged using MRI in week 12. After the last MRI session, mice were**
171 **euthanized and prepared for histology.**

172

173 **2.3 Data analysis**

174 **2.3.1 MRI data analysis**

175

176 MR images were acquired as Digital Imaging and Communication in Medicine (DICOM)
177 files, which were rescaled to retrieve the original image intensity values. The non-uniform
178 detection sensitivity associated with the use of a surface receiver coil can adversely affect
179 the registration processes. Hence, the T2W images were normalized using the
180 corresponding water phantom MR images acquired with the same parameters [20]. To
181 remove any bias that could arise due to differences in the image intensity values for the
182 different MR modalities, the images were normalised using equation (1).

$$z = \frac{(x - m)}{\sigma}$$

Equation 1

183 Where z is the new pixel value, x is the original pixel value, m is mean value of the image
184 and σ is the standard deviation of the image.

185 Apparent Diffusion Coefficient (ADC) maps were calculated by fitting the DWI data to the
186 mono-exponential equation of the Stejskal and Tanner model [21]. All data were resized to
187 match the T2W matrix (176x176). To separate the mouse brain from the background and to
188 reduce processing time, the brain area was manually delineated and separated by applying
189 an active contour method [22]. A non-linear diffusion filter was applied (No. of iterations=100,
190 Lambda=0.2, and epsilon=1) to remove noise and preserve the sharpness of the edges in
191 the image [23].

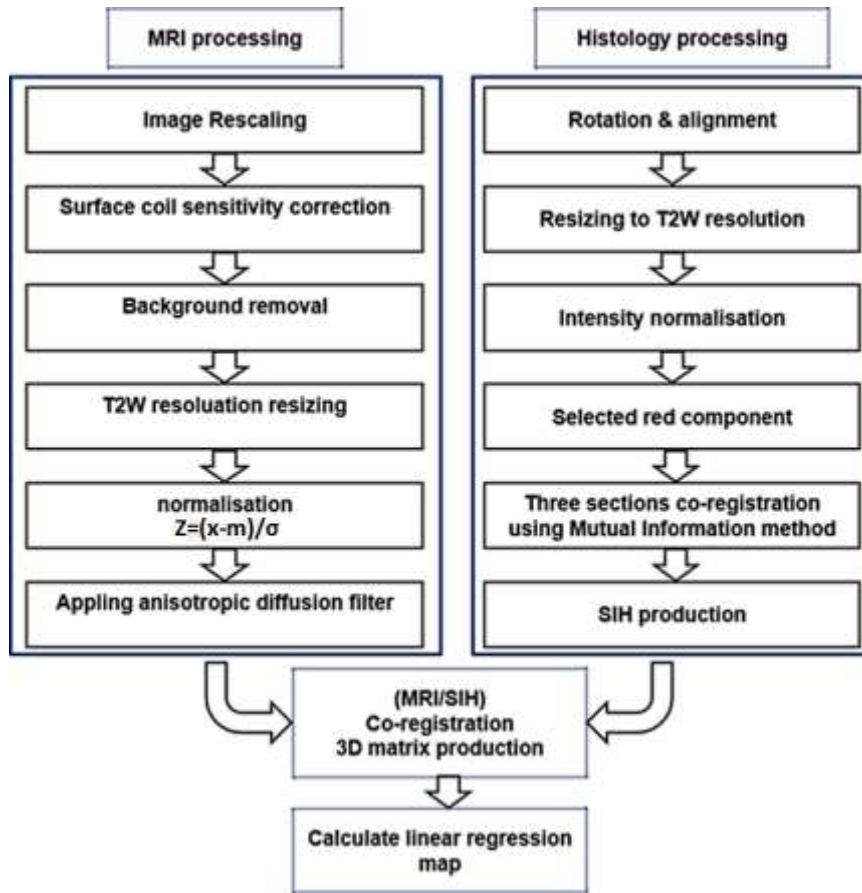
192 **2.3.2 Histology data analysis**

193
194 Mice were sacrificed immediately after the MRI session, with the brains removed and fresh-
195 frozen for 2 minutes at -45 C° using an isopentane solution tube immersed in dry ice. The
196 frozen brains were then embedded in Cryomatrix and protected in an M-1 embedding matrix
197 to prevent dehydration (Thermo Fisher Scientific, UK). Histology sections were then cut
198 manually in the same plane as the MRI, with a section thickness of 20 μm and scanned
199 using a Zeiss 710 upright confocal microscope at x10 magnification. Histology images were
200 then down-sampled from their original resolution (approximately 1400x1200 pixels) using
201 the cubic spline method (MATHLAB built-in function) to match the resolution of the
202 T2W,T2map,ADC and FA images (176x176).

203 Signal intensity inhomogeneity due to a difference in staining across the image were
204 automatically corrected for each section by using a histogram equalization method [24].
205 Further, a threshold value was selected, creating a brain mask to remove the background
206 signal. Stacked In-plane Histology (SIH) maps were generated first by co-registration of
207 multiple histology sections, then by taking a voxel-wise average of the signal intensities.
208 Registration used non-rigid Mutual Information (MI) based transformation with global
209 translation, rotation, scaling and shearing for optimal registration. In one histology section
210 with greater tissue deformations, a B-spline method was applied to improve the registration.
211 For more details regarding the SIH methodology and histology pre-processing, see Mubarak
212 et al [19]. The flow chart below (Fig.3) summarizes the image processing steps for both MRI

213 and SIH. All datasets in this work were processed using in-house MATLAB script (MATLAB
 214 R2020a).

215



216

217

218

219 **Figure 3: Pipeline shows MRI and histology image processing steps which allows for co-registration**
 220 **MR images and SIH to create IRM and IRMave.**

221

222 2.4 Multiple Linear Regression

223

224 Regression is widely used in the medical field to understand the degree of relation or
 225 association between continuous variables. The most common class of regression is linear
 226 regression, which attempts to describe the relationship between dependent variable Y and
 227 the independent variable X with a straight line, as in Equation 2.

$$Y = w_0 + w_1 X$$

Equation 2

228

229 To identify the optimal combination of the different MRI modalities, we applied a multiple
230 linear regression model containing interaction terms, which can be written as

$$Y = w_0 + w_1 X_1 + w_2 X_2 + w_3 X_3 + w_4 X_1 X_2 + w_5 X_1 X_3 \dots \dots \dots \quad \text{Equation 3}$$

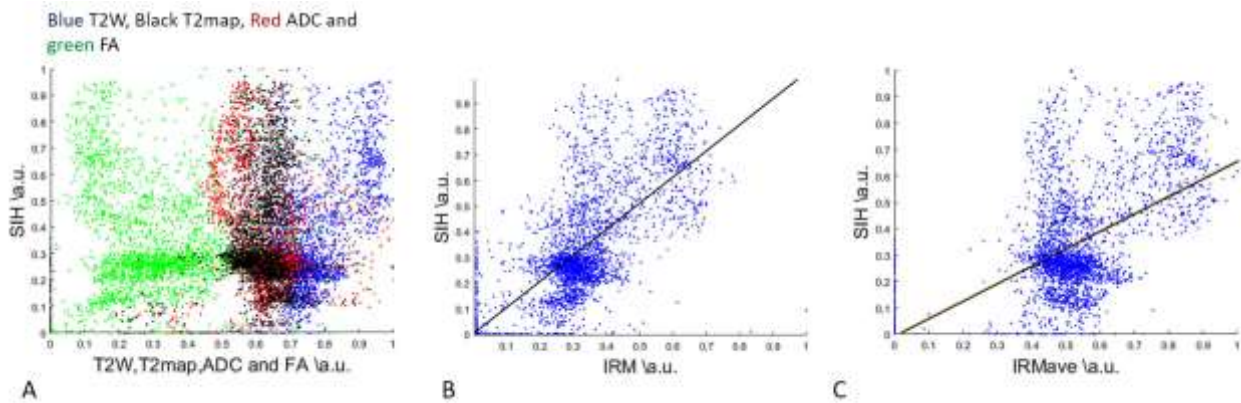
231

232 Where the dependent variable Y represents the normalized histology (SIH) value (i.e.
233 tumour map) and the independent variables X_1, X_2, X_3, X_4 represent the normalized MRI
234 parameters T2W, ADC, FA, T2map. Multiple regression was performed using MATLAB
235 R2020a with a built-in function (Regress)

236 Initially, this interaction regression method, (equation 3), was applied to the MRI/histology
237 data of each individual mouse, giving the optimal set of w_i values for each mouse. This set
238 of w_i values were then re-applied to equation 3, along with the MRI data (X_1, X_2, X_3, X_4), to
239 produce a single tumour map (Y) for that mouse, which we termed the interaction regression
240 map (IRM) (Fig. 5). As this interaction regression map (IRM) for a particular mouse, is
241 constructed from the MRI/histology data for that mouse, it is to be expected that it
242 approaches the ground truth histology (SIH).

243 However, in order to test the multi-parametric hypothesis, that a combination of the MRI
244 images can better identify the tumour than the individual images, a common set of w_i values
245 is needed. This common set of w_i values was taken as the average of the w_i values obtained
246 from the individual mice. For each mouse, this set of averaged w_i values and the MRI data
247 (X_1, X_2, X_3, X_4), were applied to equation 3, to produce a single tumour map (Y) for that mouse,
248 which we termed the average interaction regression map (IRM_{ave}), (Fig. 5).

249 Figure 4a shows the relationship between normalized SIH values and the individual MRI
250 modalities (T2W, T2map ADC and FA). Figure 4b shows that the scatter plot of individual
251 voxels' SIH values against the IRM value for an individual mouse has a positive correlation
252 (0.62). Figure 4c, shows a scatter plot for the same animal, of SIH verse IRM_{ave}.



253

254 **Figure 4: (A) Scatter plot shows SIH values vs. T2W, T2map, ADC and FA values. (B) Scatter plot**
 255 **shows SIH values against IRM after applying linear regression modal. (C) Scatter plot shows SIH values**
 256 **against IRM_{ave} values.**

257 3. Statistical Analysis

258

259 The performance of the multiple linear regression analysis was evaluated using three
 260 statistical methods:

261 **1.** The Pearson coefficient, which is used to identify if two or more variables are related to
 262 each other. The correlation coefficient (r) is the numerical assessment of the strength of
 263 the relationship between the X and Y values in the data set consisting of (X, Y) pairs.

264 **2.** To test the accuracy of each modality of the MRI and IRM maps, tumour volumes of
 265 interest (VOI) were manually selected. These were compared to our gold standard VOI
 266 selected from the stacked in-plane histology.

267 **3.** Receiver Operating Characteristic (ROC) curve analysis was used to compare abnormal
 268 regions of interest probed by the MRI, IRM and histology [25] . A comparison of abnormal
 269 regions gives measurements of True Negative (TN), False Positive (FP), False Negative
 270 (FN) and True Positive (TP) used to calculate sensitivity, specificity, accuracy, and Dice.

271

$$\text{Sensitivity} = \frac{\text{TP}}{\text{TP} + \text{FN}} \quad \text{Equation 4}$$

$$\text{Accuracy} = \frac{\text{TP} + \text{TN}}{\text{TP} + \text{FP} + \text{FN} + \text{TN}} \quad \text{Equation 5}$$

$$\text{Specificity} = \frac{\text{TN}}{\text{TP} + \text{TN}} \quad \text{Equation 6}$$

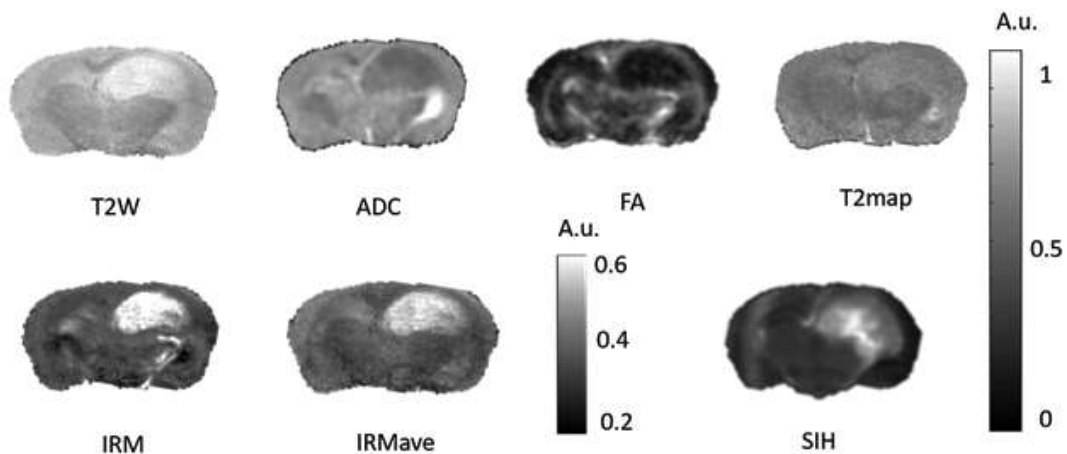
$$\text{Dice} = \frac{2 * \text{TP}}{\text{FP} + \text{FN} + 2 * \text{TP}} \quad \text{Equation 7}$$

272 Using Graph Pad prism 6 (Ver.6.01, 2012), all data were analyzed using ANOVA and the *t*-
 273 test to compare abnormal tumour-related regions in both MRI and histology images. All
 274 values are reported as mean ± standard deviation (STD).

275 4. Results

276

277 Qualitative and quantitative assessments were used to evaluate the individual MRI
 278 modalities and the regression maps. One of the qualitative methods was a visual
 279 comparison. Figure 5 shows a comparison between the individual images (T2W, ADC, FA,
 280 and T2map) and the interaction regression maps (IRM and IRMave). This comparison
 281 shows a significant improvement in tumour region detection as well as the detection of the
 282 infiltration of tumour cells beyond the edema when using IRM rather than individual MR
 283 images.



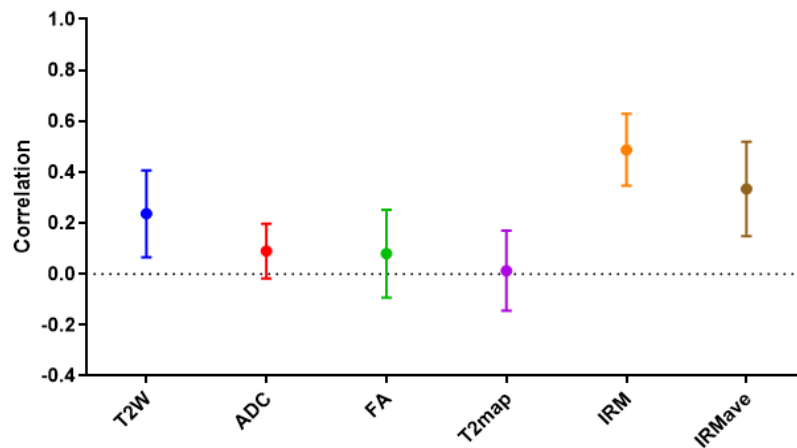
284

285 **Figure 5: Comparison of original MR images (T2W, ADC, FA, and T2map), linear regression maps (IRM,**
 286 **IRMave) and SIH.**

287

288 The stacked in-plane histology (SIH) provides a 'ground truth' for a quantitative assessment
 289 of the individual MRI modalities and the interaction regression maps (IRM and IRMave). As

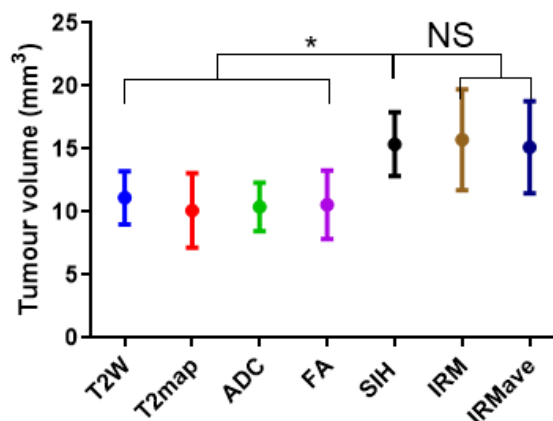
290 the MRI data has been co-registered with the SIH, each MRI voxel has a corresponding
 291 'ground-truth' SIH voxel (example scatter plots are shown in figure 4). This allows correlation
 292 coefficient analysis between individual MRI modalities, IRM / IRM_{ave} and the SIH 'ground
 293 truth'. Figure 6 illustrates that IRM ($r>0.5$), and IRM_{ave} ($r>0.3$) had higher correlation
 294 coefficient values than T2W, ADC, FA, and T2map. Statistically, the following clinically
 295 relevant r values were used: an r value less than 0.4 was considered poor, an r value of 0.4-
 296 0.59 was considered fair, an r value of 0.6-0.74 was considered good, and an r value greater
 297 than 0.74 was considered excellent [26].



298

299 **Figure 6: The Pearson correlations between individual MRI (T2W, ADC, FA and T2map), IRM, IRM_{ave}**
 300 **against SIH in the brain after discarding the background.**

301



302

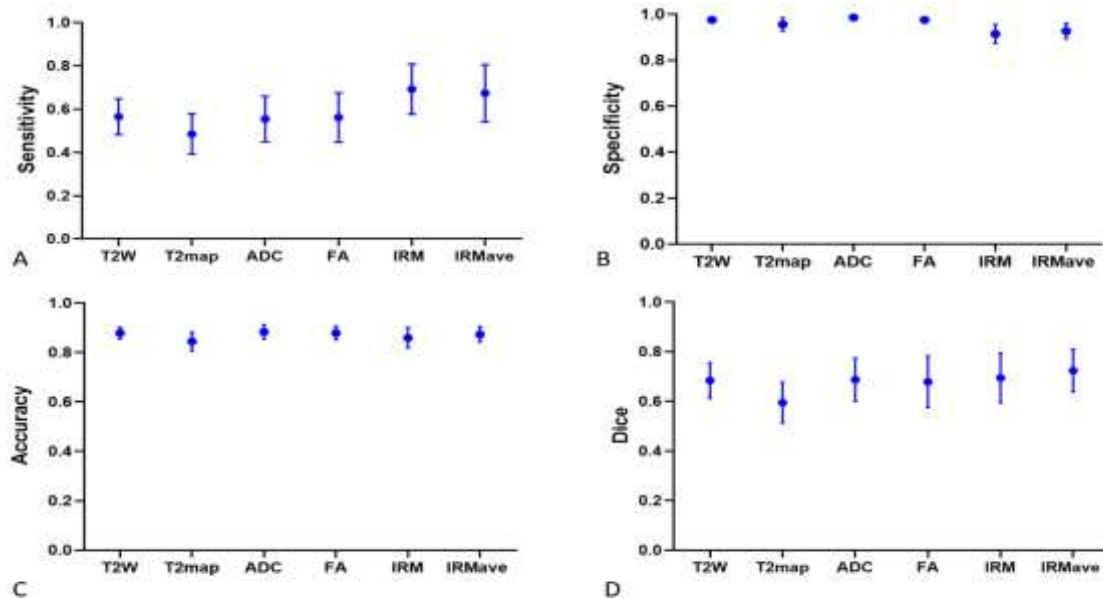
303 **Figure 7: Volumetric tumour comparison between interaction regression maps and SIH. All tumour**
 304 **volumes are represented by mean ± STD manually delineated from the individual MRI maps and the**
 305 **interaction regression maps at week 12. Also shown is the tumour volume manually delineated from**
 306 **histology (SIH). ANOVA and t-test were used and showed statistical significance ($P<0.0125$) between**
 307 **T2W, ADC, FA, and T2map and SIH and no statistical significance ($P>0.025$) between IRM and IRM_{ave}.**

308

309 Volumetric analysis is also a powerful tool for studying tumours and the effects of cancer
310 treatment. However, in this study, we compared tumour volumes identified using individual
311 MRI modalities, interaction regression maps and histology (SIH) to ascertain the benefits of
312 the interaction regression method. The tumour VOIs for nine mice (one did not develop a
313 tumour) were obtained by manual delineation by two observers, each with more than 3
314 years' experience. Figure 7 shows the tumour volumes measured from the four MRI
315 modalities, the Interaction regression maps and the histology (SIH). The mean tumour
316 volumes selected by IRM ($15.73 \pm 3.9 \text{mm}^3$) and IRM_{ave} ($15.14 \pm 3.64 \text{mm}^3$) exhibited no
317 statistically significant difference when compared with the SIH mean volume ($15.3 \pm$
318 2.54mm^3). Whereas there was a significant difference in mean tumour volumes measured
319 by the individual MRI modalities compared to the mean volume measured using the 'ground
320 truth' SIH maps

321 ROC analysis was employed to evaluate the accuracy of detection of the tumour region.
322 This method included four scenarios: true positives (TP) and true negatives (TN), where the
323 identification between MRI and histology regions was correct, and false positives (FP) and
324 false negatives (FN), where differences existed between the MRI and histology regions.

325 Figure 8A shows the sensitivity of both individual MRI modalities and interaction regression
326 maps. The high sensitivity of interaction regression maps indicates that they are more
327 sensitive to detecting the tumour burden than individual MRIs. Figure 8B shows that
328 specificity is indicative of accurate tumour detection. The slightly higher specificity values of
329 individual MRIs when compared with those of interaction regression maps may be due to
330 individual MRIs being totally inside the histology tumour region. There was no significant
331 difference between individual MRIs and interaction regression maps with respect to
332 accuracy and Dice values (Fig.8C-D).



333

334 **Figure 8: ROC analysis between MRI, interaction regression maps and SIH which enables evaluation**
 335 **of the accuracy of detection of the tumour region compared with SIH (A) Sensitivity (B) Specificity**
 336 **(C) Accuracy (D) Dice.**

337

338

339

340 5. Discussion

341

342 5.1 Glioblastoma and multi-parametric MRI

343 GBM is the most common and aggressive primary brain tumour, with a median survival time
 344 of 10.6 months after diagnosis [27]. GBM cells can progressively infiltrate neighboring
 345 normal brain regions [13, 14]. It is widely acknowledged that conventional MRI (T1W, T2W,
 346 ADC, Gd-T1) cannot detect GBM infiltration beyond the contrast enhanced region of Gd-T1
 347 images. However, changes beyond the contrast enhanced region have been detected with
 348 MRS [28], MRI measurements of cerebral blood volume (CBV) [29] and cerebral blood flow
 349 (CBF)[30].

350 In recent years, the clinical research community has paid more attention to mpMRI. It is
 351 considered that the combination of image data from various MRI modalities (morphological,
 352 functional and metabolic) has the potential to provide the radiologist with a single tumour
 353 map by extracting more information from the individual images. Although the selection of
 354 MRI modalities and how they are combined is much debated. Several studies have

355 attempted to use mpMRI to detect the GBM tumour infiltrative region. Fathi Kazerooni,
356 Mohseni [3] proposed that using a combination of MRI images (ADC, PWI and T2W)
357 followed by a segmentation method could find the extent of GBM and help in its delineation
358 before surgery. Furthermore, several studies have recommended including additional
359 imaging biomarkers adopted from diffusion and perfusion modalities as a means of
360 achieving deeper insight into the physiological behavior of glial brain tumours [2, 16]. For
361 example, Jensen and Schmainda [31] stated that, by combining several MRI modalities
362 (morphological and functional) with a segmentation algorithm, they were able to distinguish
363 between the invasion of the tumour and the normal tissue inside edema. Further, a
364 combination of Dynamic Contrast Enhanced (DCE) and Dynamic Susceptibility Contrast
365 (DSC) MRI with an unsupervised segmentation algorithm showed promising results for
366 distinguishing between vasogenic edema and tumour-containing edema, which appear
367 similar in conventional MRI [32]. However, all these clinical studies lacked direct verification
368 with the commonly agreed gold standard of histology.

369 **5.2 Quantitative assessment of the multi-parametric MRI hypothesis**

370 MRI is capable of generating a range of individual image contrasts, giving morphological,
371 functional and metabolic information [33, 34]. It has long been hypothesized that better
372 diagnoses could be achieved by combining these multiple images (the so-called multi-
373 parametric (mpMRI) or multi-spectral MRI).

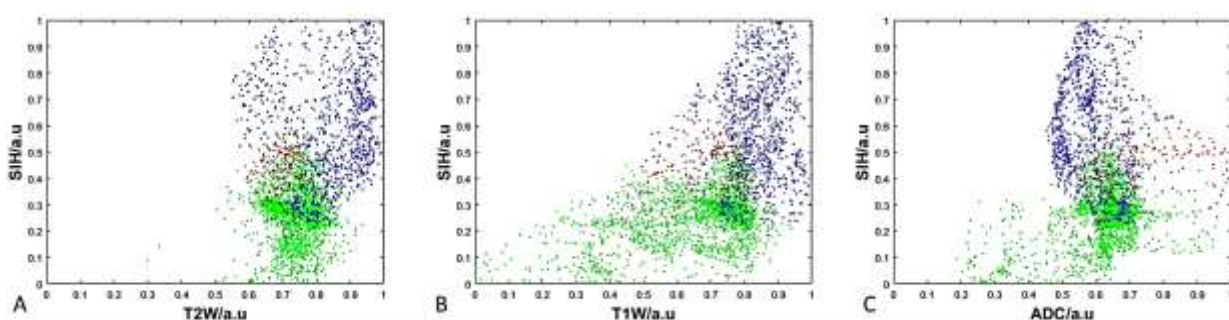
374 Here, we have sought to quantitatively test this hypothesis for the first time, using a
375 previously published dataset of co-registered MR images and histology, from a mouse
376 model of glioblastoma [18, 19]. These studies achieved high quality registration of histology
377 with MRI, not by improving on current image registration algorithms, but by focusing on
378 improving the quality of the histology used. This was done in four ways: First, a “flash-freeze”
379 method for fixation was employed instead of transcardial fixation with paraffin embedding.
380 This helps to preserve tissue morphology, reducing macroscopic distortions associated with
381 extracting, cutting, and staining. Second, the histology was cut in relatively thick 20 μ m
382 sections, to reduce the risk of tears/distortions. Third, histology sections were carefully cut
383 in the image acquisition plane (e.g. the MRI plane), guided by thin slice T2-weighted MRI.
384 Fourth, in order to better reflect the MRI slice thickness (1500 μ m), multiple in-plane histology
385 sections (20 μ m), selected from across the MRI slice thickness, were stacked and averaged.
386 This stacked in-plane histology (SIH) method allows the quantitative comparison of MRI with

387 histology. This step is particularly crucial where the pathology is heterogeneous, with
388 variations occurring on the length scale of the MRI slice thickness.

389 The immunocompromised mice were intracranially injected with G7 Glioblastoma cells,
390 which were derived from a primary human tumour cell line. The histology sections were then
391 stained for Human Leukocyte Antigen (HLA), which is very specific in the mouse model, as
392 it stains only cells that originated from the implanted human tumour cells. Hence, the HLA
393 stacked in-plane histology (SIH) provided a gold standard for characterizing the co-
394 registered MRI voxels as either normal or containing tumour cells (see fig. 9).

395 A comprehensive visual comparison between individual MRI, interaction regression maps,
396 and SIH showed that the regression maps were more visually comparable with SIH. A voxel-
397 wise correlation analysis (Fig. 6) showed a poor correlation between the individual MRI
398 modalities and normalized SIH, whereas the correlation was fair for the regression methods.
399 In addition, a statistical difference was found between tumour volumes identified by the
400 individual MRI modalities and the 'ground truth' SIH. However, there was no significant
401 difference between tumour volumes determined from the regression maps (IRM and IRM_{ave})
402 and those determined from the 'ground truth' SIH. Further, ROC analysis showed lower
403 sensitivity of individual MRI modalities than for the regression maps. This provides
404 quantitative evidence that mpMRI can better distinguish between the tumour region and
405 normal tissue, allowing better delineation of the tumour boundary including infiltration of
406 tumour cells.

407 It should be remembered that the current results were obtained at a high magnetic field
408 (7Tesla) in a mouse model of human glioblastoma infiltration. Hence, these results (e.g. w_i
409 values) cannot be directly translated to human patients in the clinic. For example, MRI
410 relaxation times and image contrast will differ at different clinical MRI field strengths (1.5 and
411 3Tesla). However, they do provide a rigorous justification for mpMRI.



412

413 **Figure 9: Voxel-wise scatter plots of normalized SIH and MRI data. A) SIH against T1W; B) SIH against**
414 **T2W; C) SIH against ADC. The SIH maps are used to define each voxel as normal tissue or containing**
415 **tumour cells; colors indicate whether MRI categorization was true positive (green), true negative (blue)**
416 **or false negative (Red).**

417

418

419 **6. Conclusion**

420 For the first time we are able to conclude that mpMRI, as hypothesized, provides more
421 information than the individual MR images. An interactive linear regression model was
422 better at identifying the whole tumour region than when using individual MR images alone.
423 Development and translation of such techniques could allow improved brain tumour
424 diagnosis, prognosis, and monitoring.

425 **Acknowledgments**

426 H. Al-Mubarak would like to thank the Ministry of Higher Education and Scientific Research of Iraq for financial
427 support. Contract grant sponsor: The Brain Tumour Charity; Contract grant number: 26/160.nt.

428 **References**

429

- 430 1. Abul-Kasim, K., et al., *Multimodal magnetic resonance imaging increases the overall diagnostic*
431 *accuracy in brain tumours: Correlation with histopathology.* South African Journal of Radiology, 2013.
432 **17**(1): p. 4-10.
- 433 2. Dominietto, M. and M. Rudin, *Could magnetic resonance provide in vivo histology?* Front Genet,
434 2014. **4**: p. 298.
- 435 3. Fathi Kazerooni, A., et al., *Multi-parametric (ADC/PWI/T2-w) image fusion approach for accurate*
436 *semi-automatic segmentation of tumourous regions in glioblastoma multiforme.* Magma, 2015.
437 **28**(1): p. 13-22.
- 438 4. M. Alegro, E.J.L.A., M. D. G. M. Martin, L. Grinberg, H. Heinsen, R. D. Lopes, E. A. Júnior, Lilla Zöllei
439 *Automating whole brain histology to mri registration: Implementation of a computational pipeline.*
440 *Computer vision and pattern recognition.* Computer Science, Engineering, Biology, 2019.
- 441 5. Yuan, C., et al., *In vivo accuracy of multispectral magnetic resonance imaging for identifying lipid-rich*
442 *necrotic cores and intraplaque hemorrhage in advanced human carotid plaques.* Circulation, 2001.
443 **104**(17): p. 2051-6.
- 444 6. Kiessling, F., Pichler, Bernd J. , *Small animal imaging basics and practical guide.* 2011, Germany:
445 Springer.
- 446 7. Cai, W.L. and G.B. Hong, *Quantitative image analysis for evaluation of tumour response in clinical*
447 *oncology.* Chronic Dis Transl Med, 2018. **4**(1): p. 18-28.
- 448 8. Hu, L.S., et al., *Multi-Parametric MRI and Texture Analysis to Visualize Spatial Histologic*
449 *Heterogeneity and Tumour Extent in Glioblastoma.* PLoS One, 2015. **10**(11): p. e0141506.
- 450 9. Wu, O., R.M. Dijkhuizen, and A.G. Sorensen, *Multiparametric magnetic resonance imaging of brain*
451 *disorders.* Top Magn Reson Imaging, 2010. **21**(2): p. 129-38.
- 452 10. Jardim-Perassi, B.V., et al., *Multiparametric MRI and Coregistered Histology Identify Tumour Habitats*
453 *in Breast Cancer Mouse Models.* Cancer Res, 2019. **79**(15): p. 3952-3964.
- 454 11. Vandenberghe, M.E., et al., *Voxel-Based Statistical Analysis of 3D Immunostained Tissue Imaging.*
455 *Front Neurosci,* 2018. **12**: p. 754.

- 456 12. Verma, R., et al., *Multiparametric tissue characterization of brain neoplasms and their recurrence*
457 *using pattern classification of MR images*. Acad Radiol, 2008. **15**(8): p. 966-77.
- 458 13. De Gooijer, M.C., et al., *An Experimenter's Guide to Glioblastoma Invasion Pathways*. Trends Mol
459 Med, 2018. **24**(9): p. 763-780.
- 460 14. Konukoglu, E., et al., *Extrapolating glioma invasion margin in brain magnetic resonance images:*
461 *suggesting new irradiation margins*. Med Image Anal, 2010. **14**(2): p. 111-25.
- 462 15. Burnet, N.G., et al., *Defining the tumour and target volumes for radiotherapy*. Cancer Imaging, 2004.
463 **4**(2): p. 153-61.
- 464 16. Chen, C., *Advances in the Biology, Imaging and Therapies for Glioblastoma*. 2011, Croatia: InTech.
- 465 17. Kao, H.W., et al., *Advanced MR imaging of gliomas: an update*. Biomed Res Int, 2013. **2013**: p.
466 970586.
- 467 18. Vallatos, A., et al., *Quantitative histopathologic assessment of perfusion MRI as a marker of*
468 *glioblastoma cell infiltration in and beyond the peritumoural edema region*. J Magn Reson Imaging,
469 2019. **50**(2): p. 529-540.
- 470 19. Al-Mubarak, H., et al., *Stacked in-plane histology for quantitative validation of non-invasive imaging*
471 *biomarkers: Application to an infiltrative brain tumour model*. J Neurosci Methods, 2019. **326**: p.
472 108372.
- 473 20. Axel, L., J. Costantini, and J. Listerud, *Intensity correction in surface-coil MR imaging*. AJR Am J
474 Roentgenol, 1987. **148**(2): p. 418-20.
- 475 21. Stejskal, E.O. and J.E. Tanner, *Spin Diffusion Measurements: Spin Echoes in the Presence of a Time-*
476 *Dependent Field Gradient*. The Journal of Chemical Physics, 1965. **42**(1): p. 288-292.
- 477 22. Caselles, V., R. Kimmel, and G. Sapiro, *Geodesic Active Contours*. International Journal of Computer
478 Vision, 1997. **22**(1): p. 61-79.
- 479 23. Demirkaya, O., M.H. Asyali, and P.K. Sahoo, *Image processing with MATLAB: applications in medicine*
480 *and biology*. 2009, USA: CRC press, Taylor and Francis group.
- 481 24. Belsare, A. and M. Mushrif, *Histopathological Image Analysis Using Image Processing Techniques: An*
482 *Overview*. Signal Image Process Int J, 2011. **3**: p. 23-36.
- 483 25. Garcia-Lorenzo, D., et al., *Review of automatic segmentation methods of multiple sclerosis white*
484 *matter lesions on conventional magnetic resonance imaging*. Med Image Anal, 2013. **17**(1): p. 1-18.
- 485 26. Oppo, K., et al., *Doppler perfusion index: an interobserver and intraobserver reproducibility study*.
486 Radiology, 1998. **208**(2): p. 453-7.
- 487 27. Lacroix, M., et al., *A multivariate analysis of 416 patients with glioblastoma multiforme: prognosis,*
488 *extent of resection, and survival*. J Neurosurg, 2001. **95**(2): p. 190-8.
- 489 28. Price, S.J. and J.H. Gillard, *Imaging biomarkers of brain tumour margin and tumour invasion*. Br J
490 Radiol, 2011. **84 Spec No 2**: p. S159-67.
- 491 29. Tourdias, T., et al., *Pulsed arterial spin labeling applications in brain tumours: practical review*. J
492 Neuroradiol, 2008. **35**(2): p. 79-89.
- 493 30. Golay, X., J. Hendrikse, and T.C. Lim, *Perfusion imaging using arterial spin labeling*. Top Magn Reson
494 Imaging, 2004. **15**(1): p. 10-27.
- 495 31. Jensen, T.R. and K.M. Schmainda, *Computer-aided detection of brain tumour invasion using*
496 *multiparametric MRI*. J Magn Reson Imaging, 2009. **30**(3): p. 481-9.
- 497 32. Artzi, M., et al., *Classification of tumour area using combined DCE and DSC MRI in patients with*
498 *glioblastoma*. J Neurooncol, 2015. **121**(2): p. 349-57.
- 499 33. Jacobs, A.H., et al., *Imaging in neurooncology*. NeuroRx, 2005. **2**(2): p. 333-47.
- 500 34. Nandu, H., P.Y. Wen, and R.Y. Huang, *Imaging in neuro-oncology*. Ther Adv Neurol Disord, 2018. **11**:
501 p. 1756286418759865.

502
503